UNDERSTANDING SPATIAL AND SPECTRAL MORPHOLOGIES OF ULTRACOMPACT H II REGIONS

Thomas Peters[1,2] and Mordecai-Mark Mac Low[3,5], Robi Banerjee[1], Ralf S. Klessen[1,4], Cornelis P. Dullemond[5]

ABSTRACT

The spatial morphology, spectral characteristics, and time variability of ultracompact H II regions provide strong constraints on the process of massive star formation. We have performed simulations of the gravitational collapse of rotating molecular cloud cores, including treatments of the propagation of ionizing and non-ionizing radiation. We here present synthetic radio continuum observations of H II regions from our collapse simulations, to investigate how well they agree with observation, and what we can learn about how massive star formation proceeds. We find that intermittent shielding by dense filaments in the gravitationally unstable accretion flow around the massive star leads to highly variable H II regions that do not grow monotonically, but rather flicker, growing and shrinking repeatedly. This behavior appears able to resolve the well-known lifetime problem. We find that multiple ionizing sources generally form, resulting in groups of ultracompact H II regions, consistent with observations. We confirm that our model reproduces the qualitative H II region morphologies found in surveys, with generally consistent relative frequencies. We also find that simulated spectral energy distributions (SEDs) from our model are consistent with the range of observed H II region SEDs, including both regions showing a normal transition from optically thick to optically thin emission, and those with intermediate spectral slopes. In our models, anomalous slopes are solely produced by inhomogeneities in the H II region, with no contribution from dust emission at millimeter or submillimeter wavelengths. We conclude that many observed characteristics of ultracompact H II regions appear consistent with massive star formation in fast, gravitationally unstable, accretion flows.

1. INTRODUCTION

Ultracompact (UC) H II regions have radii $R < 0.1$ pc and high radio surface brightness (Churchwell 2002). They have a characteristic distribution of morphologies (Wood & Churchwell 1989; Kurtz et al. 1994), and usually are found associated with one another and with compact H II regions (e.g. Welch et al. 1987; Gaume & Claussen 1990; Mehringer et al. 1993; Kim & Koo 2001). Their spectral energy distributions (SEDs) can reflect a transition from optically thin to optically thick emission, but often show an anomalous intermediate wavelength dependence (Franco et al. 2000; Lizano 2008). Recent radio continuum observations have suggested that ultracompact H II regions can contract, change in shape, or expand anisotropically over intervals of as little as ~ 10 yr (Franco-Hernández & Rodríguez 2004; Rodríguez et al. 2007; Galván-Madrid et al. 2008).

The observed brightness and size of UC H II regions require that they be ionized by massive stars of spectral type earlier than B3. If the regions were to expand at the sound speed of ionized gas, $c_i \sim 10$ km/s, they would have lifetimes of roughly 10^4 yr. Less than 1% of an OB star's lifetime of a few million years should therefore be spent within such a region, so the same fraction of OB stars should now lie within them. However, surveys find numbers in our Galaxy consistent with over 10% of OB stars being surrounded by them (Wood & Churchwell 1989; De Pree et al. 2005), or equivalently, lifetimes of $\sim 10^5$ yr if this model is correct.

A number of explanations have been proposed for this lifetime problem, including confinement in cloud cores by thermal pressure (De Pree et al. 1995; García-Segura & Franco 1996) or turbulent pressure (Xie et al. 1996), ram pressure confinement by infall (Yorke 1986; Hollenbach et al. 1994) or bow shocks (Van Buren et al. 1990; Mac Low et al. 1991a; Arthur & Hoare 2006), champagne flows (Bodenheimer et al. 1979; García-Segura & Franco 1996; Arthur & Hoare 2006), disk evaporation (Hollenbach et al. 1994), and mass-loaded stellar winds (Dyson et al. 1995; Redman et al. 1996; Williams et al. 1996; Lizano et al. 1996), but most have been argued to have major flaws (Mac Low et al. 2007).

We have modeled accretion on to an ionizing source using three-dimensional simulations (Peters et al. 2010, hereafter Paper I). These calculations suggest that accretion can indeed explain the lifetime problem, but in an unexpected way. Keto (2002, 2007) has argued that ultracompact and hypercompact H II regions are simply the ionized portion of an accretion flow. However, massive stars require accretion at rates exceeding 10^{-4} M$_\odot$ yr^{-1} (Beuther et al. 2002; Beltrán et al. 2006) to reach their final masses before exhausting their nuclear fuel (Keto & Wood 2006). The result is gravitational instability during collapse, leading to the formation of dense gas filaments in the rotating, collapsing flow, along with dozens of accompanying stars (Paper I). The strongest sources of ionizing radiation orbit through the dense filaments

thomas.peters@ita.uni-heidelberg.de

[1] Zentrum für Astronomie der Universität Heidelberg, Institut für Theoretische Astrophysik, Albert-Ueberle-Str. 2, D-69120 Heidelberg, Germany
[2] Fellow of the *Landesstiftung Baden-Württemberg*
[3] Department of Astrophysics, American Museum of Natural History, 79th Street at Central Park West, New York, New York 10024-5192, USA
[4] Kavli Institute for Particle Astrophysics and Cosmology, Stanford University, Menlo Park, CA 94025, U.S.A.
[5] Max-Planck-Institut für Astronomie, Königstuhl 17, D-69117 Heidelberg, Germany

repeatedly, accreting mass efficiently when they do. The filaments absorb the ionizing radiation locally, though, when this happens, shielding the rest of the H II region for long enough for it to recombine. As a result, the size of the observed H II region remains independent of the age of the ionizing star until the surrounding secondary star formation cuts off accretion on to the primary and a compact H II region begins to grow around it.

In this paper we consider in more detail than in Paper I whether our models of ionization interacting with a gravitationally unstable accretion flow can reproduce the observations of ultracompact H II regions summarized at the beginning of this section. We show how H II regions fluctuate in size as their central stars pass through density fluctuations, and demonstrate that our models qualitatively reproduce all morphologies observed for ultracompact H II regions, even giving general quantitative agreement with the distribution of different morphologies observed by Wood & Churchwell (1989) and Kurtz et al. (1994). Our models also offer a natural explanation for the observed clustering of ultracompact H II regions. We further demonstrate that they reproduce observed SEDs, and provide natural explanations for the anomalous SEDs observed for some ultracompact H II regions (Lizano 2008; Beuther et al. 2004; Keto et al. 2008).

In Sect. 2 we describe our methods for modeling ultracompact H II regions and simulating observations, while in Sect. 3 we describe the results of our work relevant for this paper. Finally, in Sect. 4 we draw conclusions.

2. NUMERICAL METHOD

2.1. *Simulations*

We present three-dimensional, gas dynamic, simulations with radiation feedback from ionizing and non-ionizing radiation. We use the FLASH adaptive-mesh code (Fryxell et al. 2000), modified to include a hybrid-characteristics raytracing method (Rijkhorst et al. 2006) to solve the radiative transfer problem. The protostars are modeled by sink particles (Federrath et al. 2010) that are coupled to the radiation module via a protostellar model (Paper I).

We simulate the collapse of a massive core with a mass of 1000 $M_\odot$. The core has constant density within the sphere with $r < 0.5\,\mathrm{pc}$, while further out the density falls off as $r^{-3/2}$. The gas temperature is initially $T = 30\,\mathrm{K}$. The core begins in solid body rotation with a ratio of rotational to gravitational energy $\beta = 0.05$.

We use an adaptive mesh with a cell size at the highest refinement level of 98 AU. Sink particles are inserted at a cut-off density of $\rho_{\mathrm{crit}} = 7 \times 10^{-16}\,\mathrm{g\,cm}^{-3}$ and accrete all gas above ρ_{crit} within an accretion radius of $r_{\mathrm{sink}} = 590\,\mathrm{AU}$ if it is gravitationally bound to the particle.

We analyze two simulations. In the first simulation (run A), we only follow the evolution of a single star and suppress the formation of any secondary stars. We do this by introducing a dynamical temperature floor

$$T_{\mathrm{min}} = \frac{G\mu}{\pi k_{\mathrm{B}}} \rho (n\Delta x)^2 \qquad (1)$$

with Newton's constant G, mean molecular weight μ, Boltzmann's constant k_{B}, local gas density ρ, and cell size Δx. This temperature floor guarantees that the Jeans length is always resolved with n cells. We must

set $n \geq 4$ to prevent artificial fragmentation (Truelove et al. 1997). In the second simulation (run B), we do not apply the temperature floor, instead allowing the formation of secondary sink particles.

More details on the simulation method as well as a detailed description of the simulation results can be found in Paper I.

2.2. *Generation of Free-Free Emission Maps*

Radio continuum emission from H II regions around massive stars at wavelengths $\lambda \geq 0.3\,\mathrm{cm}$ ($\nu \leq 10^{11}\,\mathrm{Hz}$) is predominantly caused by free-free emission from ionized hydrogen (Gordon & Sorochenko 2002). Since scattering can be neglected for this problem (Kraus 1966; Gordon & Sorochenko 2002), the equation of radiative transfer can be readily integrated. First, we calculate the free-free absorption coefficient of atomic hydrogen

$$\alpha_\nu = 0.212 \left(\frac{n_{\mathrm{e}}}{1\,\mathrm{cm}^{-3}}\right)^2 \left(\frac{T_{\mathrm{e}}}{1\,\mathrm{K}}\right)^{-1.35} \left(\frac{\nu}{1\,\mathrm{Hz}}\right)^{-2.1}\,\mathrm{cm}^{-1}, \qquad (2)$$

with number density of free electrons n_{e}, electron temperature T_{e} and frequency ν. Since the electrons thermalize quickly (Dyson & Williams 1980), we can take the gas temperature $T = T_{\mathrm{e}}$. Given the absorption coefficient, the optical depth at distance r from the edge of the domain is then

$$\tau_\nu = \int_0^r \alpha_\nu \, \mathrm{d}s. \qquad (3)$$

The radiative transfer equation in the Rayleigh-Jeans limit then leads to the brightness temperature

$$T(\tau_\nu) = \mathrm{e}^{-\tau_\nu} \int_0^{\tau_\nu} \mathrm{e}^{\tau'_\nu} T(\tau'_\nu) \, \mathrm{d}\tau'_\nu. \qquad (4)$$

The resulting map of brightness temperatures can be converted to flux densities with the solid angle subtended by the beam Ω_{S} of the telescope via

$$F_\lambda = \frac{2k_{\mathrm{B}} T}{\lambda^2} \Omega_{\mathrm{S}}. \qquad (5)$$

Following the algorithm described in Mac Low et al. (1991b), we convolve the resulting image with the beam width and add some noise according to the telescope parameters. The parameters for the Very Large Array (VLA)[6] are given in Table 1, and the parameters for the Atacama Large Millimeter Array (ALMA)[7] are given in Table 2. We model the synthetic observation using an effective Gaussian beam rather than doing a full-fledged simulation of aperture synthesis.

2.3. *Generation of Dust Emission Maps*

For the wavelengths with $\lambda \leq 0.3\,\mathrm{cm}$ observable by ALMA, in addition to the free-free emission we must also take into account continuum emission by dust particles. We use RADMC-3D[8] to generate dust emission maps as well as maps of combined free-free and dust emission from the simulation data.

---

[6] http://www.vla.nrao.edu/astro/guides/vlas/current/node11.html
[7] http://www.eso.org/sci/facilities/alma/observing/specifications/
[8] http://www.mpia.de/homes/dullemon/radtrans/radmc-3d/index.html

TABLE 1
VLA TELESCOPE PARAMETERS.

VLA band	wavelength (cm)	beam width (arcsec)	sensitivity (mJy)
4	400	24	160
P	90	6.0	4.0
L	20	1.4	0.061
C	6.0	0.4	0.058
X	3.6	0.24	0.049
U	2.0	0.14	1.0
K	1.3	0.08	0.11
Q	0.7	0.05	0.27

NOTE. — The VLA can observe at eight bands with wavelengths from 400 cm to 0.7 cm. The beam width is given in terms of the FWHM and measured in arcsec, the sensitivity is measured in in mJy. The integration time is 10 min.

TABLE 2
ALMA TELESCOPE PARAMETERS.

ALMA band	wavelength (mm)	beam width (arcsec)	sensitivity (mJy)
3	3.1	0.034	0.019
4	2.1	0.023	0.022
5	1.6	0.018	0.411
6	1.25	0.014	0.044
7	0.95	0.011	0.079
8	0.7	0.008	0.272
9	0.45	0.005	0.411

NOTE. — ALMA can observe at seven bands with wavelengths from 3.1 mm to 0.45 mm. The beam width is given in terms of the FWHM and measured in arcsec, the sensitivity is measured in mJy. The integration time is 10 min.

RADMC-3D is an AMR-based radiative transfer package for continuum and line radiative transfer. It has an interface for PARAMESH (MacNeice et al. 2000), the AMR grid library of FLASH. We use RADMC-3D for two tasks. First, to compute the dust temperature self-consistently, using the standard Monte Carlo method of Bjorkman & Wood (2001), combined with Lucy's method of treating optically thin regions (Lucy 1999). Second, to compute the images of the free-free and dust continuum emission by using it as a volume-rendering ray-tracer tool. RADMC-3D is the successor of the RADMC code (Dullemond & Dominik 2004) which has been used in numerous papers.

RADMC-3D has been tested against the earlier 2D version of RADMC for various 1D and 2D test cases. A detailed discussion of RADMC-3D will be published separately, but since this is the first scientific use of the code, we show the results of a simple test case here. It involves a simple 1D spherically symmetric envelope around a star. The density of the envelope is $\rho_{\rm dust}(r) = \rho_0(r/1{\rm AU})^{-2}$, where ρ_0 takes the values 10^{-15} g cm^{-3} for test case 1 and 10^{-14} g cm^{-3} for test case 2. The inner radius lies at 5 AU, the outer radius at 100 AU. The star has solar parameters, but we treat the stellar spectrum as a blackbody of $T = 5780$ K. For the opacity we use silicate dust spheres of 0.1 μm, using optical constants of olivine from the Jena database[9], but we artificially set the scattering opacity to zero in order to be able to compare our results to the results from a simple 1D variable eddington factor dust radiative transfer code called TRANSPHERE[10]. With RADMC-3D we now compute the dust temperature using the Monte Carlo method. We do this in two ways. First, we use a spherical 1D grid, similar to what we use for TRAN-

SPHERE. Secondly, we use a 3D Cartesian AMR-refined grid, where the refinement is done with the criterion that the cells with centers having radii $r > 5$ AU from the star should have a size $\Delta x \geq 0.2r$. This is a relatively coarse resolution, meant to test the effect of low resolution on the results. The outcome of this comparison is displayed in Figure 1, showing the excellent agreement between the temperature profiles.

3. RESULTS

Our simulations follow the gravitational collapse of the initial massive clump and lead to the formation of high-mass stars. The collapse leads to the formation of a massive rotationally flattened structure, which is gravitationally unstable and fragments. Only a single star is allowed to form in run A. It accretes $72M_\odot$ in 145 kyr. In run B, three high-mass stars with $M \geq 10M_\odot$ form within 70 kyr, and become the dominant source of ionizing radiation within the star cluster. The interaction of the ionizing radiation with the infalling accretion flow leads to multiple effects observable in both spatial and spectral diagnostics.

3.1. *Time Evolution*

The most striking property of the resulting H II regions is their extremely high variability in time and shape. In the online material of Paper I we presented movies of radio continuum maps from different viewpoints. The radio maps were generated for VLA parameters at a wavelength of $\lambda = 2$ cm, using a beam with full width at half maximum of $0\rlap{.}''14$ and a noise level of 10^{-3}Jy. The assumed distance was 2.65 kpc. All the movies show the continuous build-up and destruction of UC H II regions. The timescale for changes of more than 5000 AU in size can be as short as 100 yr.

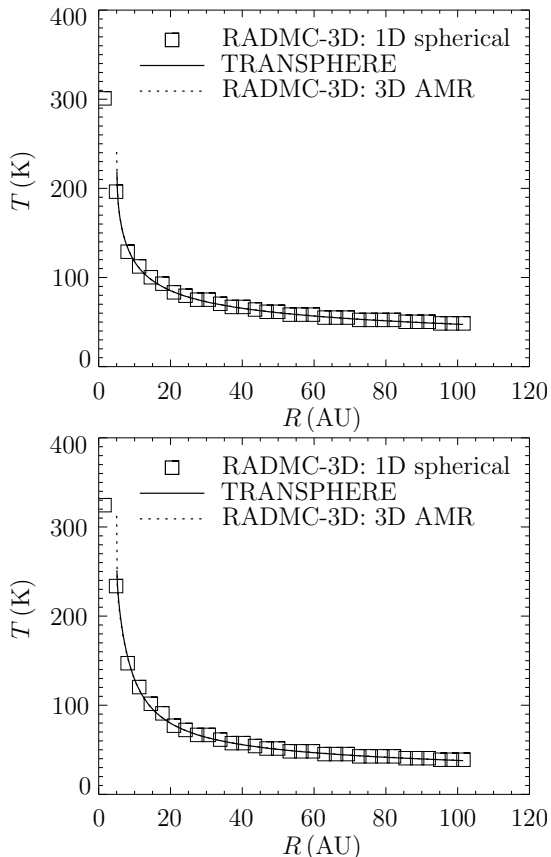This flickering is caused by the accretion flow in which the sources are embedded. When the protostar passes

FIG. 1.— Temperature profiles for two different core densities, $\rho_0 = 10^{-15}\,\mathrm{g\,cm^{-3}}$ (*left*), $\rho_0 = 10^{-14}\,\mathrm{g\,cm^{-3}}$ (*right*), as generated by TRANSPHERE, RADMC-3D on a spherical 1D grid, and RADMC-3D on a 3D AMR grid. All profiles agree with each other.

through dense, gravitationally unstable filaments in the accretion flow, they absorb its ionizing radiation, so that the gas above the filament recombines and cools down. Since the gravitational instabilities cause the accretion flow to be chaotic, the interplay between the radiation feedback and the infalling material results in highly stochastic ionization and recombination processes in the surrounding gas.

This effect is demonstrated in Figure 2. It shows dramatic changes in the H II region around the most massive star in run B. Between $t = 0.6592\,\mathrm{Myr}$ and $t = 0.6595\,\mathrm{Myr}$ (within 300 yr), a region with a diameter of $\sim 6000\,\mathrm{AU}$ suddenly recombines. Changes like this not only affect the physical size of the H II region, but they can also alter their morphology. From $t = 0.6668\,\mathrm{Myr}$ to $t = 0.6671\,\mathrm{Myr}$ (again within 300 yr), the morphology of the UC H II region surrounding the most massive protostar changes from shell-like to core-halo because of a large-scale recombination event that clears the rim of the shell. The shielding by the filaments also controls how ionizing radiation can escape perpendicular to the disk. For example, this reverses the cometary H II region around the star between $t = 0.6524\,\mathrm{Myr}$ and $t = 0.6534\,\mathrm{Myr}$ (within 1000 yr). The three examples given in Figure 2 indicate that the morphology of ultracompact H II regions around accreting massive protostars depends sensitively on accretion events close to the protostar.

The flickering observed in the simulations also resolves

the long-standing lifetime problem for UC H II regions (Wood & Churchwell 1989). Since UC H II regions are not freely expanding bubbles of gas that monotonically increase in size, their diameter does not depend on their age. An extreme version of the discrepancy between protostellar mass and size of the H II region occurs in run A, where the $70 M_\odot$ protostar has almost no visible H II region. It is totally quenched by the strong accretion flow.

While the source in run A never stops accreting, the most massive stars in run B finally stop growing when the gas reservoir around them is fully exploited. As the density surrounding the most massive star then drops, the hot, ionized gas can finally expand monotonicially, eventually overrunning the second most massive star as well. Once there is no more high-density gas in its neighborhood, the flickering around the most massive star stops. The ionized gas continues to expand, forming a compact H II region with larger size and fainter emission than the preceding ultracompact phase. We stress that it is not the ionizing radiation that stops the accretion flow by driving away the surrounding gas, rather it is the subsiding accretion flow that allows the ionized gas to expand. We call this process fragmentation-induced starvation, a more detailed discussion of which we presented in Paper I.

3.2. *Morphology*

The extended H II regions found in the simulations display a large amount of substructure. Equation (2) shows that the emission from free-free transitions scales with the square of the number density of free electrons, n_e. This explains the emission peak close to the protostar, where very dense gas in the accretion flow gets partially ionized. However, not all emission peaks are associated with stars.

Figure 3 shows some examples. The upper left panel (a_1) shows an H II region with a shell-like structure. The shell clearly exhibits a peak on its rim that is several 1000 AU away from any nearby star. The shell is created by dense shocks running through the H II region, which are replenished by material from the accretion flow. The emission of this dense gas is what creates the shell. Another example is shown in the lower left panel (a_2) of Figure 3. It shows a dense blob of gas that is externally irradiated by a massive star and creates a peak that appears to indicate the position of a second star. Obviously, peaks in emission maps are not an ideal guide to the coordinates of stars.

The aforementioned shocks contribute largely to the emission seen in the maps. The middle panels (b_1) and (b_2) in Figure 3 show an edge-on view of the rotationally flattened structure of the star cluster. The upper panel (b_1) shows that the most massive star has created a cometary H II region. The lower panel (b_2) displays the same region 200 yr later. The ionizing radiation has blown away gas from the accretion flow close to the protostar. This shock runs away from the star and creates a filament of strong emission across the H II region. The right-hand plots (c_1) and (c_2) in Figure 3 show the same region face-on. From this viewing angle, the shock shows up as shell-like structure. This demonstrates that the shell does not trace the edge where the ionizing radiation hits the accretion disk, but rather shocks generated
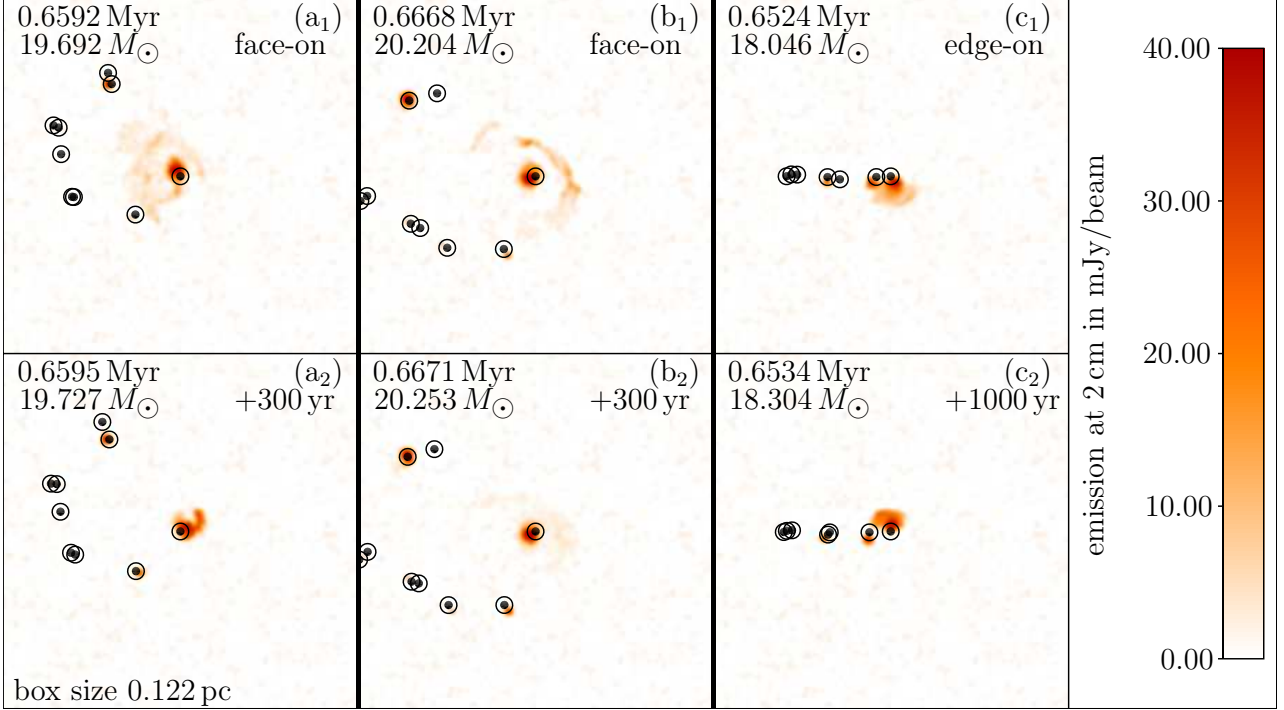
FIG. 2.— Changes in the H II region around the most massive protostar in run B. The images in the lower panels show the H II region at a slightly later time than the images in the upper panels. The left-hand panels (a_1) and (a_2) show the recombination of ionized gas with a diameter of $\sim 6000\,\mathrm{AU}$ within 300 yr. The midway panels (b_1) and (b_2) demonstrate how the morphology of the H II region changes from shell-like to core-halo in 300 yr. The right-hand panels (c_1) and (c_2) present the reversal of a cometary H II region in 1000 yr. The box size displayed is 0.122 pc. Black dots and circles indicate the position of all protostars with their accretion radii in the image. The mass of the central protostar is indicated in the images. All maps are simulated VLA observations at 2 cm with an assumed distance to the star cluster of 2.65 kpc.

from inflowing gas. The shell-like structures around accreting protostars can be interpreted as indirect evidence for the accretion process.

The origin of the shell morphology changes when accretion ceases. Figure 4 shows the late-stage evolution of the star cluster. The most massive star has stopped accreting, allowing its H II region to begin to expand quickly into the ambient gas. The left-hand plots and show the expanding H II region face-on in the upper panel (a_1) and edge-on in the lower panel (a_2). Here, the strong shell-like emission clearly comes from the dense gas in the rotationally flattened structure around the protostar rather than from a shock launched by the protostar.

While the accretion onto the most massive star has stopped and cannot directly affect the structure of the growing H II region any more, it can still be influenced by other stars that interact with the gas. Two such events occur in run B and are shown in Figure 4. The middle panels (b_1) and (b_2) show a time sequence of a $7.8 M_\odot$ star approaching the rim of the shell. Its ionizing radiation is strong enough to create sufficient thermal pressure to blow away the rim of the shell from its direct neighborhood. The right-hand panels (b_3) and (b_4) show the same star 8200 yr later, when it has already entered the compact H II region. Now its ionizing radiation can freely expand. The gravitational attraction of the star is strong enough to pull along a dense stream of gas. This stream allows the star to grow in mass although it has entered the H II region filled with underdense gas. This suggests that deformed shells could be indicative of stars inside large-scale H II regions.

3.3. Dependence of Morphologies on Viewing Angles

The simulation data presented here offer the unique opportunity to look at the same H II region from different viewing angles. We have already seen that the observed morphology depends crucially on the position of the observer. We investigate this observation in detail for some H II regions appearing in run B.

Figure 5 displays an H II region around the most massive star in run B. The first panel (a_1) shows the region face-on, and the successive panels show the region rotated around an axis in the plane of the rotationally flattened structure by $18°$ increments until a rotation of $90°$ is reached. Hence, the last panel (a_6) shows the region edge-on. This sequence of images demonstrates that a region with a shell-like morphology from one viewing angle can have a cometary morphology from a different viewing angle.

The transition angle at which the shell-like morphology turns into a cometary morphology is about $72°$ in this particular case. The online material for this article contains a movie of the volume-rendered (logarithmic) absorption coefficient of this region along with the corresponding synthetic VLA image as the line of sight is rotating, illustrating the complex structure of the ionized gas in the H II region, and how it determines the morphology, depending on the viewing angle.

Because the ultracompact H II region shape is asymmetric, we get a different result if we perform the rotation around a different axis. Figure 6 starts with the last frame (a_6) of Figure 5 and successively rotates the region by $90°$ around the polar axis. This means that the
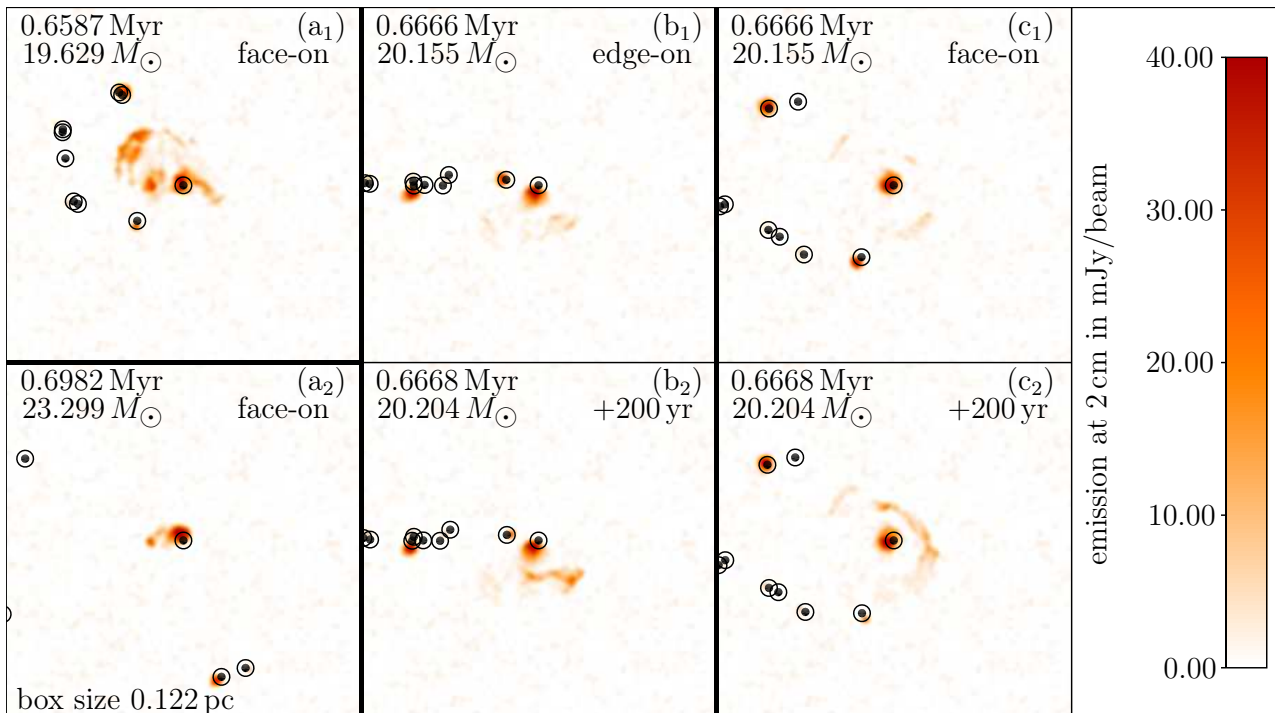
FIG. 3.— Emitting structures around the most massive protostar in run B. The left-hand panels (a$_1$) and (a$_2$) give two examples of emission peaks that are not directly related to stars. This calls into question the usual understanding that coordinates of stars should be directly related to emission peaks. The middle panels (b$_1$) and (b$_2$) show an edge-on view of the star cluster with a cometary H II region around the most massive star. Within 200 yr, a shock is launched at the protostar, runs through the H II region and creates a filamentary structure. The right-hand panels (c$_1$) and (c$_2$) show the situation face-on. Here, the shock looks like a shell expanding from the protostar. This indicates that the appearance of H II regions is closely related to accretion events close to the protostar. Black dots and circles indicate the position of all protostars with their accretion radii in the image. The mass of the central protostar is indicated in the images. All maps are simulated VLA observations at 2 cm with an assumed distance to the star cluster of 2.65 kpc.

view is edge-on for all times. At an angle around 36°, the cometary region develops strong shell-like structures. We already know that these filaments have their origin in gas blown away by the protostar. This region is of shell-like type since it is bounded by a dense filament. This means that shell-like regions can occur both at face-on and at edge-on view. In principle, the same holds true for cometary regions. They can also be observed face-on when the ionizing radiation is shielded anisotropically.

We have repeated the same exercise for different H II regions and find that the transition angle between shell-like and cometary morphologies shows no systematic behavior. Figure 7 shows two more rotations from face-on to edge-on. We show only the first and last images as well as the transition angle. The upper panels (a$_1$) to (a$_3$) show the transformation of a shell-like morphology into a cometary morphology at $t = 0.6864$ Myr, the lower panels (b$_1$) to (b$_3$) show a similar transition at $t = 0.6925$ Myr. The central star has a mass of $22.532 M_\odot$ and $23.025 M_\odot$, respectively. The transition angle is about 36° in the former and 54° in the latter case. They depend on the details of the structure. A universal angle above which transition occurs does not exist.

3.4. *Morphology Statistics*
3.4.1. *Types*

Morphologies of UC H II regions were classified by Wood & Churchwell (1989) and Kurtz et al. (1994) as shell, cometary, core-halo, spherical, irregular and unresolved. De Pree et al. (2005) abandoned the core-halo

morphology and introduced a new bipolar category for elongated H II regions. They argued for abandoning the core-halo type because most H II regions are surrounded by faint emission, which produces a halo around any H II region. Though this may be true, we find it useful to keep this morphological type for regions with a pronounced central peak and a fainter envelope. The presence of a pronounced envelope clearly distinguishes this morphology from the spherical type, which we also find.

In addition, we do not require shell-like regions to be void of central peaks. Although the larger, late-time shells do indeed not have central peaks, the UC H II regions associated with accreting protostars do have central peaks because they ionize their own accretion flow. In fact, observations with high sensitivity and resolution do find centrally peaked shells that were previously classified as spherical (Carral et al. 2002). We predict that more regions of this type will be found as observations with better resolution and sensitivity also become available for more distant massive star forming regions.

Figure 8 demonstrates the importance of resolution and sensitivity in identifying the correct morphology. The figure shows synthetic maps of the same shell-like H II region for VLA parameters at 2 cm, placed at different distances to the observer. The shell disappears between 6 and 10 kpc, where both the spatial resolution and the noise level make it impossible to distinguish between parts of the H II region and pure noise. On the other hand, the number of centrally peaked shells seen in our simulations might be reduced by including additional feedback processes like line-driven stellar winds or mag-
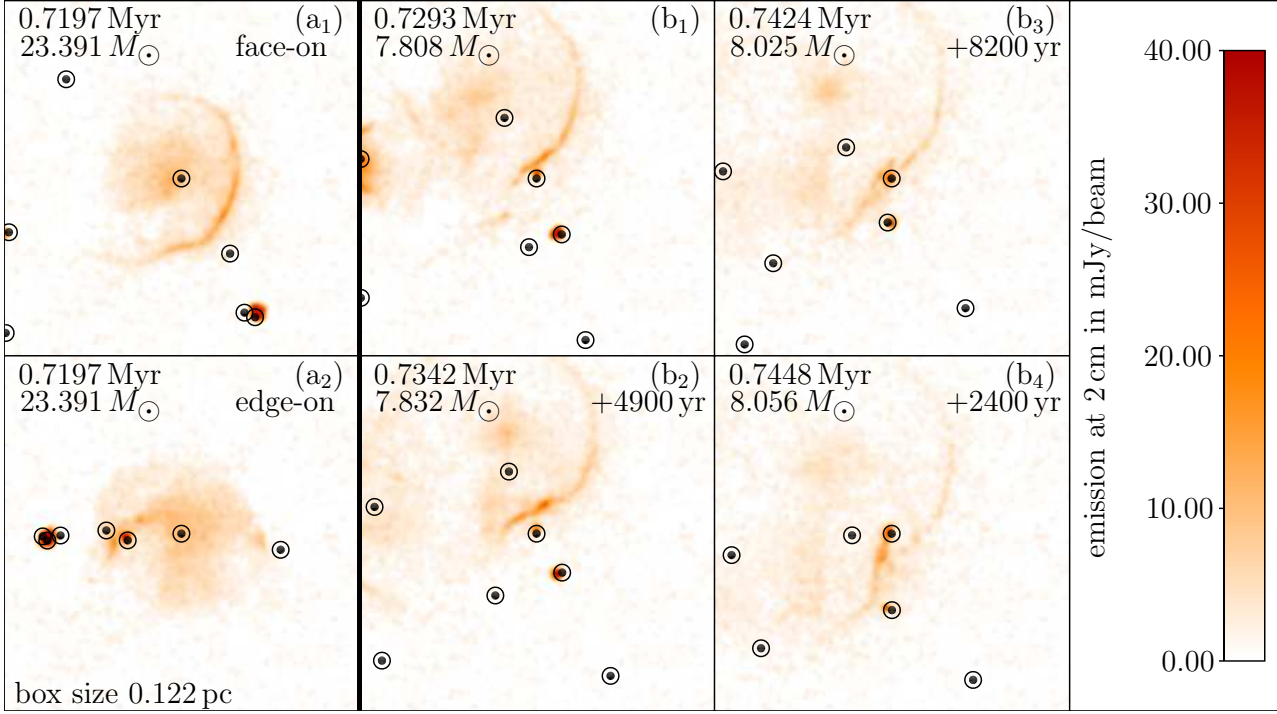
FIG. 4.— Compact H II region created by the most massive protostar in run B. The left-hand panels show this region face-on in the upper panel (a₁) and edge-on in the lower panel (a₂). The emission in the shell has its origin in the rotationally flattened structure around the protostar and not in a shock running through the H II region. The middle and right-hand panels (b₁) to (b₄) show a time sequence of a second star interacting with the dense gas that bounds the region. In the middle panels (b₁) and (b₂), this star blows away a dense filament by its own ionizing radiation. The right-hand panels (b₃) and (b₄) demonstrate what happens when it enters the low density region. Its gravitational field pulls a dense stream of gas behind it. Broken-up shells could thus be a helpful observational signature to locate stars inside H II regions. Black dots and circles indicate the position of all protostars with their accretion radii in the image. The mass of the central protostar is indicated in the images. All maps are simulated VLA observations at 2 cm with an assumed distance to the star cluster of 2.65 kpc.
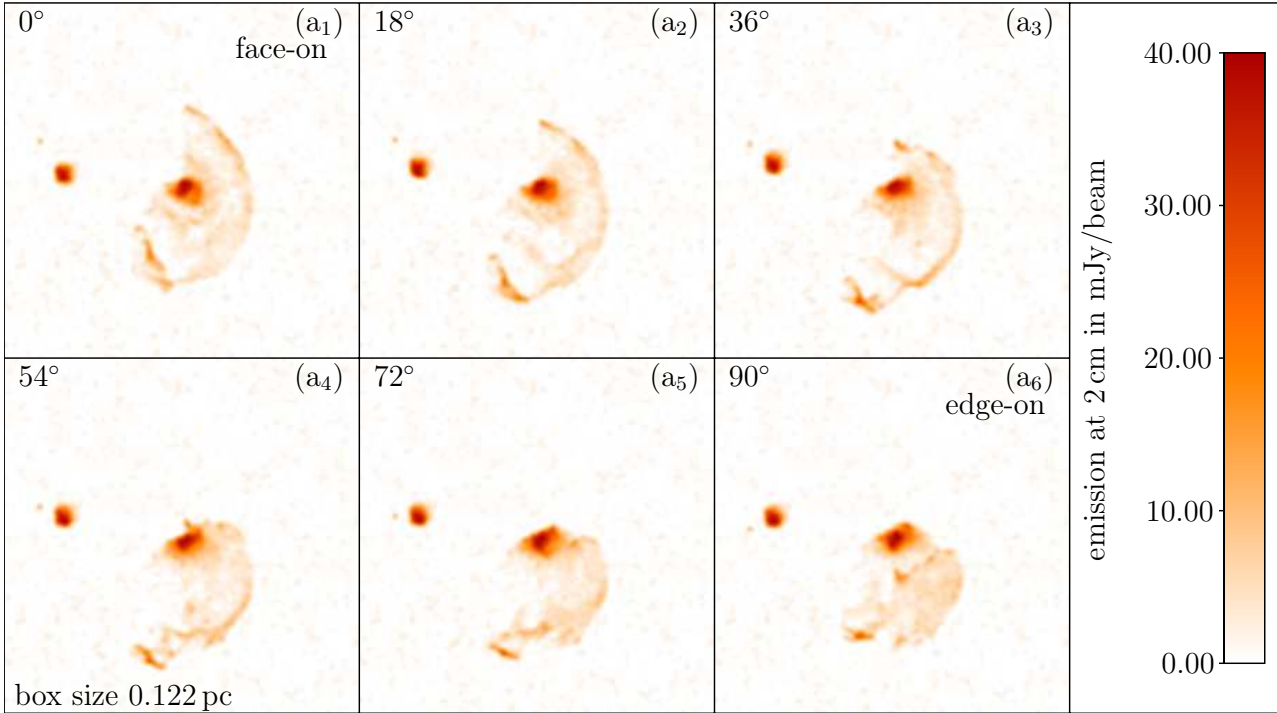
FIG. 5.— H II region in run B around a star with $22.956 M_\odot$ at $t = 0.6907$ Myr. The view in the first panel (a₁) is face-on. The subsequent panels show rotations by $18°$ increments around an axis in the plane of the rotationally flattened structure. The last panel (a₆) shows the region edge-on. At an angle of about $72°$, the morphology has turned from shell-like into cometary. All maps are simulated VLA observations at 2 cm with an assumed distance to the star cluster of 2.65 kpc.
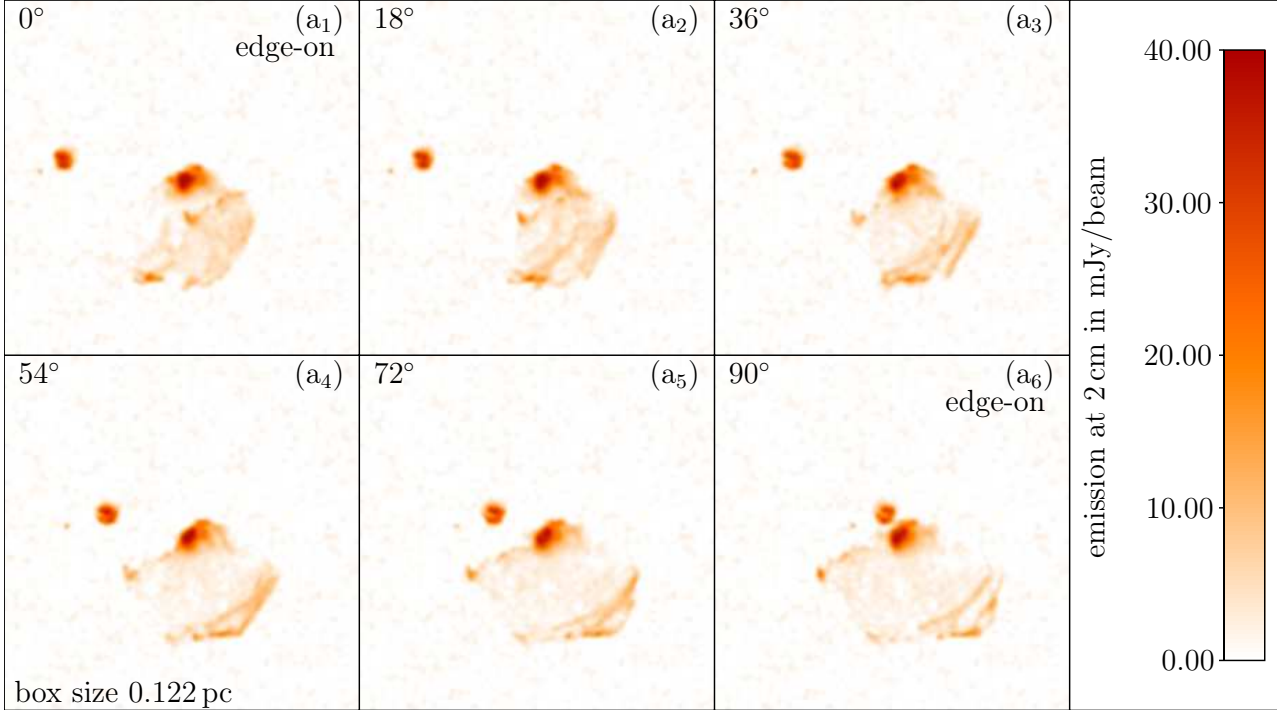
FIG. 6.— H II region in run B around a star with $22.956 M_\odot$ at $t = 0.6907$ Myr. The first panel (a_1) is identical with the last panel (a_6) of Figure 5. The region is successively rotated around the polar axis, so that the view is edge-on for all angles. The morphology changes from cometary to shell-like at about $36°$. All maps are simulated VLA observations at 2 cm with an assumed distance to the star cluster of 2.65 kpc.
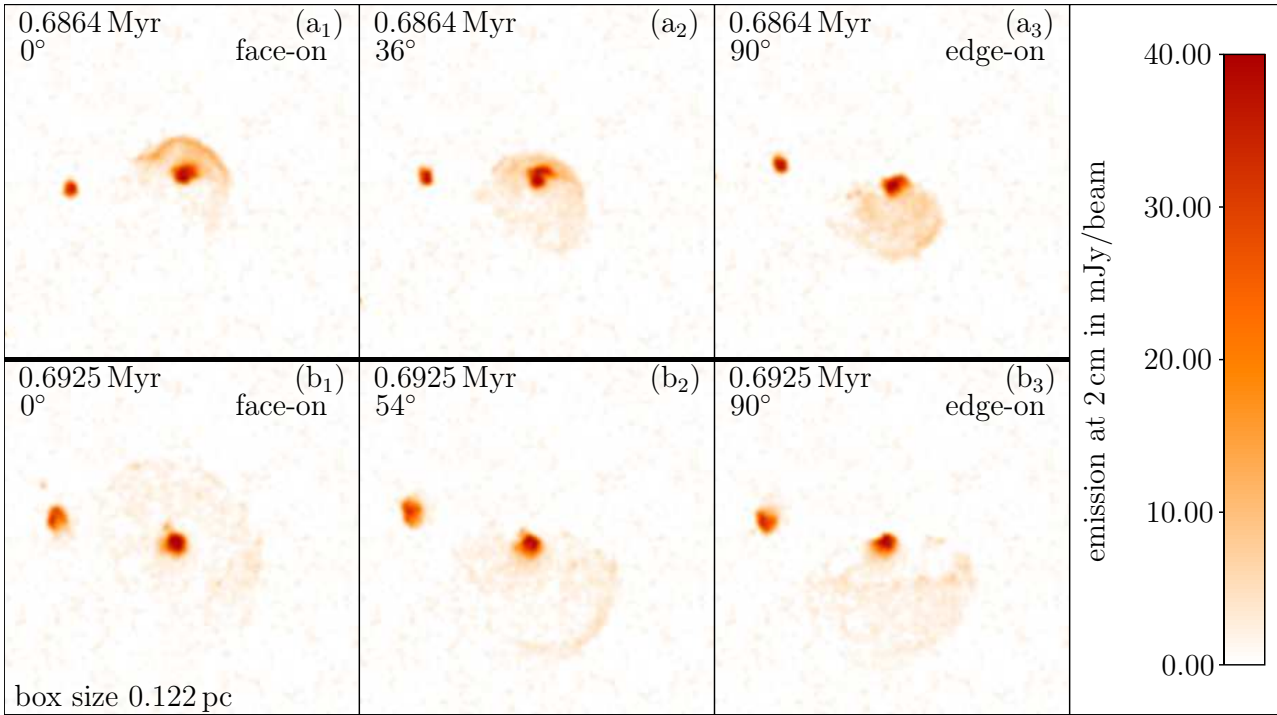

FIG. 7.— H II regions in run B that show different transition angles from shell-like to cometary. The upper panels (a_1) to (a_3) show an H II region at $t = 0.6864$ Myr around a $22.532 M_\odot$ star, the lower panels (b_1) to (b_3) at $t = 0.6925$ Myr when the star has $23.025 M_\odot$. The polar transition angles are $36°$ and $54°$, respectively. All maps are simulated VLA observations at 2 cm with an assumed distance to the star cluster of 2.65 kpc.

netically driven outflows, which might be able to create a cavity around the protostar. If these processes would be strong enough to thin out the dense accretion flow sufficiently to remove the peaks remains an open question.

The new bipolar type is not well defined. De Pree et al. (2005) gave only one example for this new category, where the bipolar shape is not very distinctive. Churchwell (2002) required an hourglass shape for the bipolar morphology, which is not present in their example. Although we do find morphologies that look bipolar in the simulations, there are only very few of them, and their features are not very pronounced. The small number of bipolar regions is in agreement with observations (Churchwell 2002; De Pree et al. 2005). All of the bipolar regions could equally well fall into one of the other classes, which is why we do not take this category into account.

The sensitive dependence on viewing angle and the high time variability of the H II region caused by the accretion flow is sufficient to produce morphologies of any described type in a single simulation. Figure 9 shows maps from run A with only one ionizing source. The displayed shell-like and core-halo morpholgies are face-on views, whereas the cometary H II region is viewed edge-on. As discussed above, the same morphologies can equally well be obtained at different viewing angles. It is apparent that the size of the H II region does not scale with the mass of the protostar. On the contrary, the irregular region corresponds to the largest protostar, but it is among the smallest H II regions.

3.4.2. *Comparison to Observations*

For comparison with the observational surveys by Wood & Churchwell (1989) and Kurtz et al. (1994), we perform a census of morphologies in run A and run B. We select 25 snapshots from each simulation and view each one from 20 randomly chosen angles. This gives a total of 500 images per simulation. The different viewing angles take into account the fact that because of the axisymmetric geometry of the initial conditions, some morphologies preferentially occur at different orientations. For example, shell-like morphologies are found mostly face-on, and cometary morphologies edge-on. The set of different viewing angles, uniformly distributed on the unit sphere around the center of the computational domain, avoids statistical biases by this effect. By the same token, the distribution of morphologies also changes with time. Since many stars in run B reach a mass of $10\,M_\odot$ by the end of the simulation, the later times contain more spherical and unresolved H II regions than the beginning of the simulation. Since we do not know the geometry and the evolutionary stage of the UC H II regions in the surveys, we assume randomly distributed orientations and ages and thus average over different viewing angles and simulation snapshots to get a representative sample. We note that this somewhat overstates the contribution from later stages in our simulations, since with a standard IMF there are probably far more star forming events that terminate with the formation of low-mass OB stars than higher-mass ones. To achieve consistency with the observational analysis techniques we use contour plots to identify the morphological classes and follow the definitions given in Wood & Churchwell (1989).

To guarantee that the viewing angles are distributed

TABLE 3
PERCENTAGE FREQUENCY DISTRIBUTION OF MORPHOLOGIES

Type	WC89	K94	Run A	Run B
Spherical/Unresolved	43	55	19	60 ± 5
Cometary	20	16	7	10 ± 5
Core-halo	16	9	15	4 ± 2
Shell-like	4	1	3	5 ± 1
Irregular	17	19	57	21 ± 5

NOTE. — Percentage relative frequencies of UC H II region morphologies in surveys and simulations. The table shows the morphology statistics of UC H II regions in the surveys of Wood & Churchwell (1989) (WC89) and Kurtz et al. (1994) (K94) as well as from a random evolutionary sample from run A and run B of 500 images for each simulation. For run B, the mean value and standard deviation of the relative frequencies from independent evaluations by the first four co-authors are given. The statistics for run A, in which only one massive star forms, disagree with the observations.

evenly on the sphere, we use a rejection method to calculate the random angles (Press et al. 1986). We start with three random numbers x, y, z with a uniform distribution on the interval $[-1, 1]$. We then calculate the radius $r = \sqrt{x^2 + y^2 + z^2}$ and drop all points with $r > 1$. The remaining points are projected onto the sphere, $X = x/r$, $Y = y/r$ and $Z = z/r$. The Cartesian coordinates (X, Y, Z) of the point on the unit sphere are then converted into spherical coordinates (ϑ, φ), resulting in the desired distribution of viewing angles.

The results of our statistical analysis are presented in Table 3. The numbers from run B are taken from evaluations performed independently by the first four authors, so that we can give mean values and standard deviations for the relative frequencies. The standard deviations remained small in absolute terms, never exceeding five percentage points, although some are large in relative terms, particularly for the rarer types.

Given the variation amongst the observational surveys, the results from the multiple sink simulation run B are quite consistent with the observational numbers. In particular, we find that roughly half of the sample represents spherical or unresolved UC H II regions, in agreement with the classical lifetime problem. Conversely, the results show that the relative numbers of spherical and unresolved H II regions in run A disagree by more than 20 percentage points with the observational findings.

This result clearly disagrees with theoretical models in which massive stars form alone. Since the protostar in run A grows very quickly, it cannot generate such a large number of strongly confined H II regions. Instead, lots of irregular H II regions form. The only way to get a large number of spherical and unresolved H II regions is the formation of a stellar cluster. This again shows that run B is a much more realistic model for massive star formation.

3.5. *Emission and Optical Depth*

It is interesting to study the appearance of H II regions at different wavelengths. Since the optical depth of the free-free radiation calculated from the simulation data is exactly known, we can investigate how morphological features of H II regions depend on the optical depth. As an example, we examine in detail the H II region from the upper panels (a_1) to (a_3) of Figure 7 at $t = 0.6864\,\mathrm{Myr}$ around a $22.532 M_\odot$ star in run B.
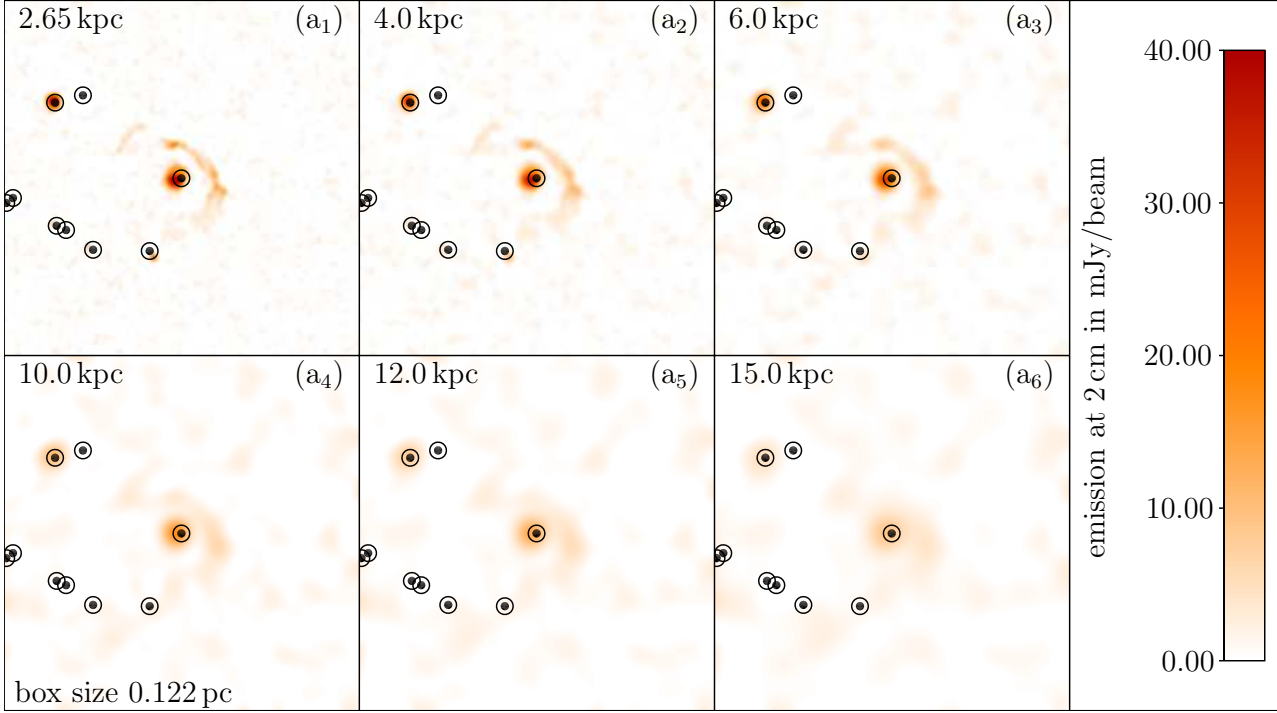
FIG. 8.— Shell-like H II region of run B with a central peak placed at different distances to the observer. The synthetic 2 cm VLA maps show that the shell-like feature disappears between 6 and 10 kpc. To detect it at such large distances, observations with higher spatial resolution and sensitivity are required. Black dots and circles indicate the position of all protostars with their accretion radii in the image.
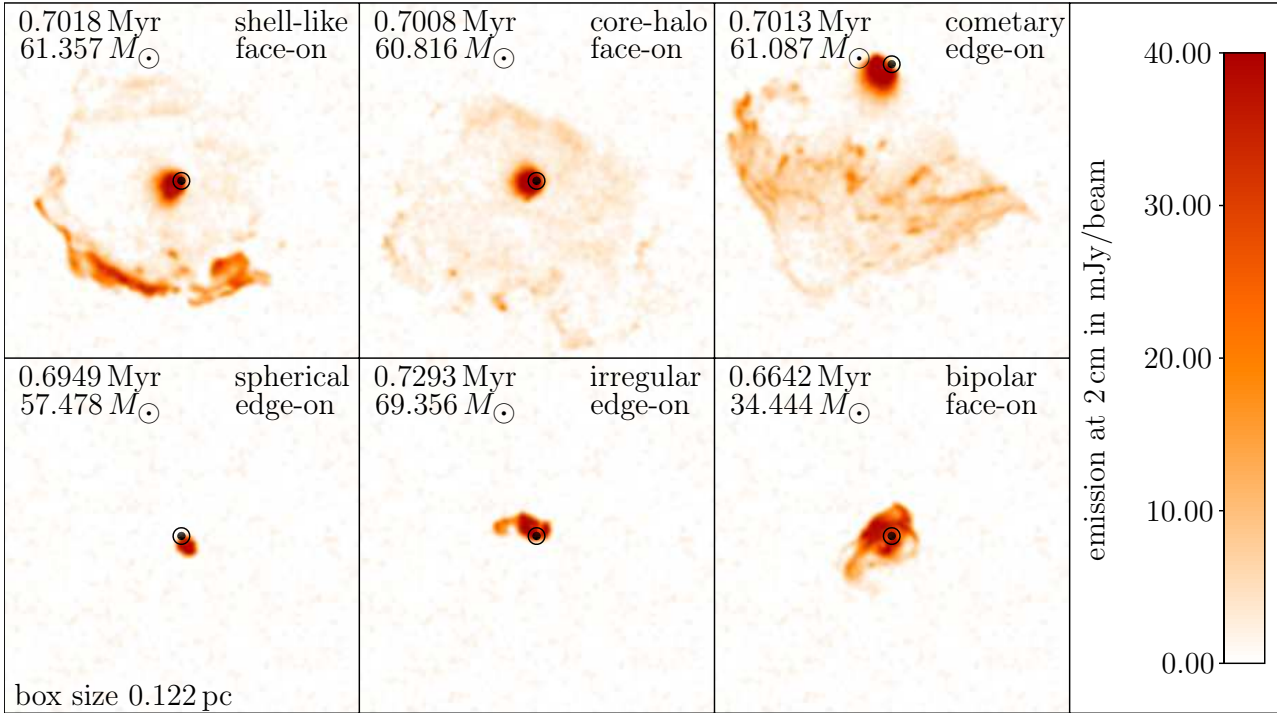

FIG. 9.— Different morphologies observed in run A, which has only a single ionizing source (central black dot). All morphologies found in surveys are present, depending on the simulation time and the viewing angle. The lower right panel demonstrates the problem with the bipolar category. The region is clearly elongated, but it also shows a shell-like structure. Since elongation alone seems to be insufficient to define a category on its own, we do not consider bipolar regions as a separate category. All maps are simulated VLA observations at 2 cm with an assumed distance to the star cluster of 2.65 kpc.

Figure 10 shows synthetic VLA observations for wavelengths from 20 cm to 0.7 cm assuming a distance of 2.65 kpc (see Tab. 1). The beam width decreases with wavelength, so that the H II region is increasingly better resolved. The corresponding images of optical depth are shown in Figure 11. In agreement with the expected behavior evident from Equation (2), the optical depth decreases with decreasing wavelength. The broad peak at 20 cm appears not only because of the large beam, but also because the whole H II region is optically thick. At 6 cm, only the right-hand side of the H II region is optically thick, as is clearly visible in the VLA observation. At 3.6 cm, only a small region around the protostar and in an arc-like feature is optically thick, which leads to a shell-like H II region. The VLA maps at 3.6 and 2 cm look similar, but at the smaller wavelength the shell is not optically thick anymore. The one-to-one correspondence between emission features and optically thick regions breaks at 2 cm. For 1.3 and 0.7 cm, the optically thick region around the protostar disappears. The shell is still visible at these wavelengths.

3.6. Millimeter and Submillimeter Maps

At millimeter and submillimeter wavelengths one generally expects to observe dust emission along with the free-free emission. This is not the case for the rather low mass core in the model presented here. Since the total initial gas mass in our model is only $1000 \, \mathrm{M_\odot}$, there is less than $10 \, \mathrm{M_\odot}$ of dust in the whole domain during the simulation, under the assumption of a canonical gas-to-dust ratio of 100. This is not enough to produce any observable emission, because the free-free radiation is much stronger. Hence, the simulated ALMA maps of this model show only free-free emission, but not dust.

We can estimate the maximum flux due to dust emission as follows. Let M_{dust} be the total dust mass, d the distance to the source, κ_ν the dust opacity and $B_\nu(T)$ the black-body spectrum for the temperature T. Then the total flux from all dust is approximately

$$F_\nu = \frac{1}{d^2} M_{\mathrm{dust}} \kappa_\nu B_\nu(T). \qquad (6)$$

To arrive at an estimate for the upper limit of F_ν, we set $d = 2.65 \, \mathrm{pc}$, $M_{\mathrm{dust}} = 10 \, \mathrm{M_\odot}$, $T = 1000 \, \mathrm{K}$ and $\kappa_\nu = 8 \times 10^{-2} \, \mathrm{cm^2 g^{-1}}$ at $\nu = 187 \, \mathrm{GHz}$ ($\lambda = 1.6 \, \mathrm{mm}$). This yields $F_\nu \approx 25.5 \, \mathrm{Jy}$ or, assuming an UC H II region with 0.03 pc diameter, 1.8 mJy/beam for an effective beam width of 0.018 arcsec. This is only a factor of 4 larger than the noise level for a 10 min integration time of this ALMA band (see Table 2), which is 0.41 mJy. Though this calculation demonstrates that the small amount of dust in our simulation would already be very faint when free-free emission was absent, what really makes the dust emission invisible is its weakness compared to free-free emission (see also Section 3.7), which is independent of the telescope sensitivity.

We caution, however, that the above calculation assumes a homogeneous distribution of dust across the H II region. This treatment neglects dust emission from an accretion disk around the massive star, which we cannot resolve in our simulation and may produce significant dust emission. In our numerical example, ALMA would be able to resolve these disks, if they exist, and detect their dust emission. A similar argument holds for disks

around low-mass stars that are being exposed to ionizing radiation from a neighboring high-mass star, which may life long enough to be observed (Hollenbach et al. 1994; Richling & Yorke 1998). This caveat also applies to the spectral energy distributions in the submillimeter regime (see Section 3.7).

We demonstrate the absence of dust emission in Figure 12 with the H II region shown in Figure 10. The bright shell that was visible at VLA wavelengths completely disappears as the wavelength gets shorter. Instead, bright spots directly at the location of the massive stars appear. This emission is caused by partially ionized, dense gas of the accretion flow around these massive stars. None of the images shows any appreciable dust emission.

3.7. Spectral Energy Distributions

A useful diagnostic of UC H II regions is their integrated SED. For a medium at constant temperature, the integral in Equation (4) for the brightness temperature leads to

$$T(\tau_\nu) = T(1 - \mathrm{e}^{-\tau_\nu}). \qquad (7)$$

In the frequency regime where the emission is dominated by free-free, Equations (2) and (5) show that the flux F_ν of a homogeneous source typically grows as ν^2 in the optically thick regime (small frequencies) and falls off like $\nu^{-0.1}$ in the optically thin regime (large frequencies). For typical emission measures of $\mathrm{EM} = 10^8 \, \mathrm{pc \, cm^{-6}}$, the transition frequency for which $\tau = 1$ is $\nu_{\mathrm{t}} \approx 5.3 \, \mathrm{GHz}$. This turnover frequency depends only weakly on the emission measure, $\nu_{\mathrm{t}} \propto \mathrm{EM}^{0.48}$.

However, many observed SEDs of H II regions do not behave in this simple manner but show anomalous scaling exponents (Lizano 2008). In particular, there are SEDs that grow linearly with ν over a frequency interval that can be as large as the whole VLA range (see Table 1). Such anomalous scaling exponents can be reproduced by H II region models with ionized gradients (Panagia & Felli 1975; Olnon 1975; Franco et al. 2000; Avalos et al. 2006; Keto et al. 2008), hierarchical clumps (Ignace & Churchwell 2004) and additional dust emission (Rudolph et al. 1990; Pratap et al. 1992; Beuther et al. 2004; Keto et al. 2008).

The data from our numerical simulations is certainly more realistic than the simple ionized gradient or hierarchical clump models. Therefore it is reassuring that we can reproduce the typical shapes of observed SEDs. We show two examples in Figure 13. The left-hand SED shows the full coverage from VLA over ALMA to IRAS frequencies for the H II region of Figures 10 and 12. The SEDs show the typical shape of those reported in Wood & Churchwell (1989). As already noted above, the free-free radiation is by far dominant up to ALMA frequencies. For IRAS frequencies, however, dust emission is the dominant process. The right-hand SED shows another example that more nicely illustrates the typical scaling behavior expected for the free-free emission. The dotted lines grow $\propto \nu^2$, the dashed lines fall off $\propto \nu^{-0.1}$.

One example of an SED with an anomalous scaling $\propto \nu^1$ (solid line) is shown in Figure 14. The result can be a combined effect of density gradients in the ionized gas as well as shadowing by clumps, just as in the simpler analytical models. We do not need any dust to pro-
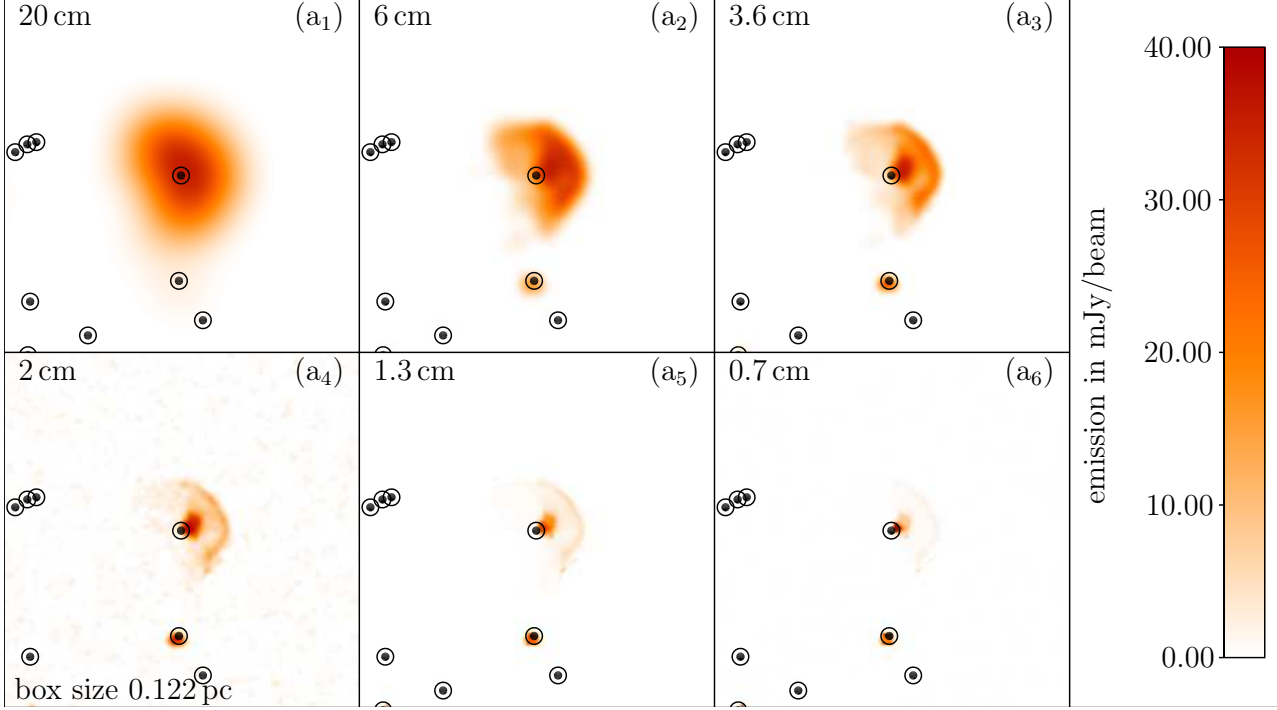
FIG. 10.— H II region in run B around a $22.532 M_\odot$ star at $t = 0.6864\,\mathrm{Myr}$ for different VLA bands. The beam width decreases with decreasing wavelength, so that the H II region is inceasingly better resolved. The assumed distance to the observer is 2.65 kpc. Black dots and circles indicate the position of all protostars with their accretion radii in the image.
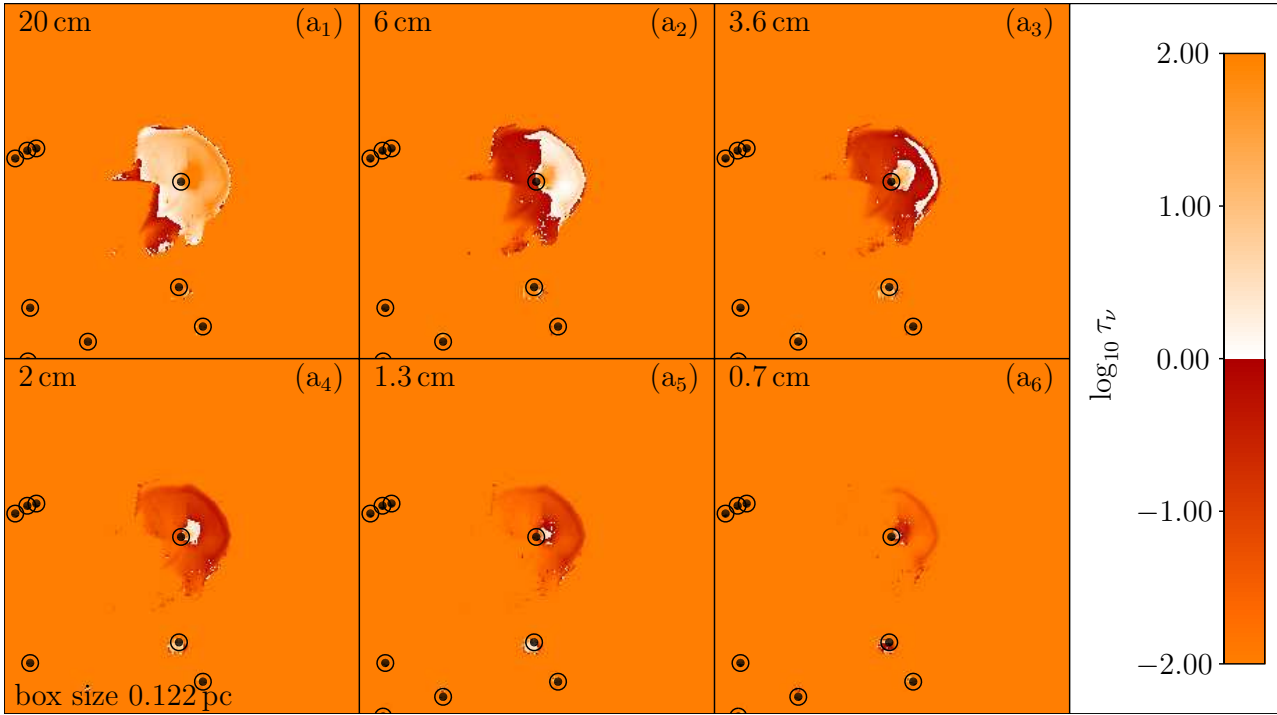

FIG. 11.— The same H II region as in Figure 10. The images show the optical depth of free-free radition at the different VLA bands. With decreasing wavelength, the H II region becomes dominantly optically thin. The color scale is chosen with a sharp break at optical depth unity, so that the transition between the optically thick and thin regimes can be easily identified. Black dots and circles indicate the position of all protostars with their accretion radii in the image.
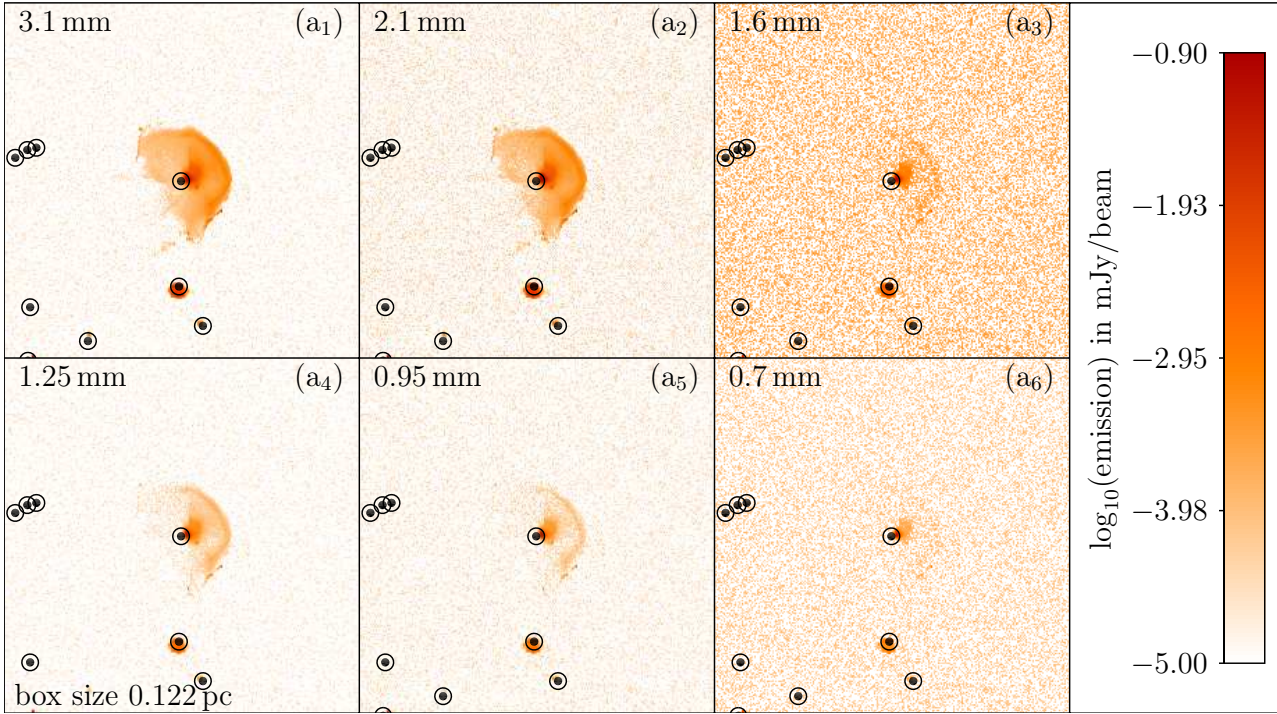
FIG. 12.— The H II region from Figure 10 at ALMA wavelengths. Note that the color scale is logarithmic, different from the linear scale in Figure 10. At high frequencies, only bright spots close to the massive stars are visible. These images show no dust emission since it is too weak compared to free-free emission. This is because our whole simulation box contains less than $10\,\mathrm{M}_\odot$ of dust. Black dots and circles indicate the position of all protostars with their accretion radii in the image.

FIG. 14.— Anomalous SED from an H II region in run B. The dotted line shows a scaling $\propto \nu^2$, the dashed line a scaling $\propto \nu^{-0.1}$ and the solid line a scaling $\propto \nu^1$. The free-free emission of this region grows anomalously with a spectral index around unity across the full VLA and most of the ALMA coverage. This scaling is produced solely by density inhomogeneities, not by dust emission. Missing crosses representing dust emission are below the flux range shown in the image. The assumed distance is 2.65 kpc.

FIG. 13.— SEDs from H II regions in run B. The plots show full SEDs from VLA to IRAS frequencies. The dotted lines scale $\propto \nu^2$ and the dashed lines scale $\propto \nu^{-0.1}$. The agreement of the free-free emission with the expected power laws is different for the two regions. Dust emission is visible only in the IRAS range. Missing crosses representing dust emission are below the flux range shown in the image. The assumed distance for both SEDs is 2.65 kpc.

duce anomalous exponents, and in fact in our particular model, the dust emission is so low that it is unable to produce such gradients. Hence, our simulations reproduce both the general shape of H II regions SEDs as well as the observed anomalous scaling behavior entirely with the computed distribution of ionized gas.

4. CONCLUSIONS

We have presented synthetic continuum observations of the H II regions formed in our collapse simulations of massive star formation described in Paper I. We find that the H II regions are highly variable in size and shape as long as the massive star continues accreting. Dense filaments in the gravitationally unstable accretion flow irregularly shield ionizing radiation from the central star. This shielding effect leads to a large-scale ($\sim 5000\,\mathrm{AU}$) flickering of the H II regions on timescales as short as $\sim 100\,\mathrm{yr}$. As long as the flickering continues, there is no direct relation between the age of the star and the size of the H II region. This result appears able to resolve the UC H II lifetime problem.

Furthermore, we have identified the structures inside the H II regions that produce the continuum emission. We find that emission peaks are not necesarily related to the positions of stars. Instead, strong emission is produced by partially ionized gas from the accretion flow that enters the H II region. These filaments can be ion-
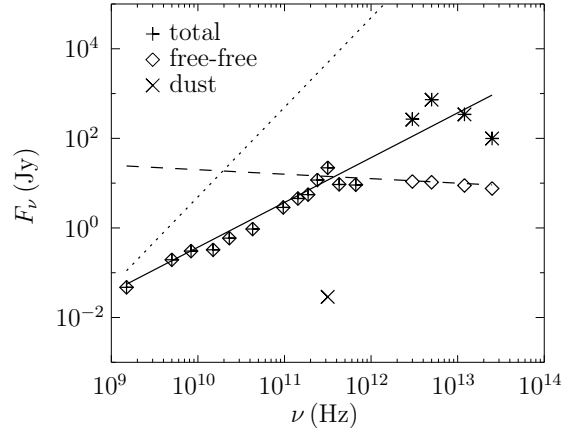
ized and blown away by thermal pressure. Since the continuum emission is determined solely by the structure of the flow field around the massive star, the appearance of the H II region depends strongly on the angle from which it is viewed. For example, we find that the same H II region can be classified as shell-like or cometary, depending on the position of the observer.

We have evaluated the distribution of apparent H II region morphologies. The multiple sink simulation run B reproduces the observed relative frequencies reported from surveys, including the high fraction of spherical or unresolved regions. The single sink simulation run A, however, fails to reproduce the morphology statistics. This is because the single star grows so quickly that it is statistically unable to produce a significant fraction of the smallest H II regions. The formation of a whole stellar cluster is necessary to get the relative frequencies of the smallest H II regions right. This analysis provides strong evidence against models of massive star formation where all or most high-mass stars form in isolation.

In addition to the H II region morphologies, we can also reproduce the different SEDs characteristic of UC H II regions. We find that our initial gas mass of $1000\,M_\odot$ is too small to produce observable dust emission at VLA or ALMA wavelengths. Nevertheless, ultracompact H II regions at different times and places in our models show SEDs with both regular transitions from optically thick to optically thin spectral slopes as well as anomalous scaling with a spectral slope around unity. These slopes are entirely produced by inhomogeneities in the density structure, with no contribution from dust. However, follow-up simulations with more massive initial clumps will be required to completely pin down the role of dust in observed SEDs.

REFERENCES

Arthur, S. J. & Hoare, M. G. 2006, ApJS, 165, 283

Avalos, M., Lizano, S., Rodríguez, L. F., Franco-Hernández, R., & Moran, J. M. 2006, ApJ, 641, 406

Beltrán, M. T., Cesaroni, R., Codella, C., Testi, L., Furuya, R. S., & Olmi, L. 2006, Nature, 443, 427

Beuther, H., Schilke, P., Sridharan, T. K., Menten, K. M., Walmsley, C. M., & Wyrowski, F. 2002, A&A, 383, 892

Beuther, H., Zhang, Q., Greenhill, L. J., Reid, M. J., Wilner, D., Keto, E., Marrone, D., Ho, P. T. P., Moran, J. M., Rao, R., Shinnaga, H., & Liu, S.-Y. 2004, ApJ, 616, L31

Bjorkman, J. E. & Wood, K. 2001, ApJ, 554, 615

Bodenheimer, P., Tenorio-Tagle, G., & Yorke, H. W. 1979, ApJ, 233, 85

Carral, P., Kurtz, S. E., Rodríguez, L. F., Menten, K., Cantó, J., & Arceo, R. 2002, AJ, 123, 2574

Churchwell, E. 2002, ARA&A, 40, 27

De Pree, C. G., Rodríguez, L. F., & Goss, W. M. 1995, Rev. Mex. Astron. Astrofís., 31, 39

De Pree, C. G., Wilner, D. J., Deblasio, J., Mercer, A. J., & Davis, L. E. 2005, ApJ, 624, L101

Dullemond, C. P. & Dominik, C. 2004, A&A, 417, 159

Dyson, J. E. & Williams, D. A. 1980, Physics of the interstellar medium (Manchester University Press)

Dyson, J. E., Williams, R. J. R., & Redman, M. P. 1995, MNRAS, 277, 700

Federrath, C., Banerjee, R., Clark, P. C., & Klessen, R. S. 2010, ApJ, 713, 269

Franco, J., Kurtz, S., Hofner, P., Testi, L., García-Segura, G., & Martos, M. 2000, ApJ, 542, L143

Franco-Hernández, R. & Rodríguez, L. F. 2004, ApJ, 604, L105

Fryxell, B., Olson, K., Ricker, P., Timmes, F. X., Zingale, M., Lamb, D. Q., MacNeice, P., Rosner, R., Truran, J. W., & Tufo, H. 2000, ApJS, 131, 273

Galván-Madrid, R., Rodríguez, L. F., Ho, P. T. P., & Keto, E. 2008, ApJ, 674, L33

García-Segura, G. & Franco, J. 1996, ApJ, 469, 171

Gaume, R. A. & Claussen, M. J. 1990, ApJ, 351, 538

Gordon, M. A. & Sorochenko, R. L. 2002, Radio Recombination Lines (Kluwer Academic Publishers Group)

Hollenbach, D., Johnstone, D., Lizano, S., & Shu, F. 1994, ApJ, 428, 654

Ignace, R. & Churchwell, E. 2004, ApJ, 610, 351

Keto, E. 2002, ApJ, 580, 980

—. 2007, ApJ, 666, 976

Keto, E. & Wood, K. 2006, ApJ, 637, 850

Keto, E., Zhang, Q., & Kurtz, S. 2008, ApJ, 672, 423

Kim, K.-T. & Koo, B.-C. 2001, ApJ, 549, 979

Kraus, J. D. 1966, Radio Astronomy (McGraw-Hill, Inc.)

Kurtz, S., Churchwell, E., & Wood, D. O. S. 1994, ApJS, 91, 659

Lizano, S. 2008, in Astronomical Society of the Pacific Conference Series, Vol. 387, Massive Star Formation: Observations Confront Theory, ed. H. Beuther, H. Linz, & T. Henning, 232–239

Lizano, S., Canto, J., Garay, G., & Hollenbach, D. 1996, ApJ, 468, 739

Lucy, L. B. 1999, A&A, 344, 282

Mac Low, M.-M., Toraskar, J., Oishi, J. S., & Abel, T. 2007, ApJ, 668, 980

Mac Low, M.-M., Van Buren, D., Wood, D. O. S., & Churchwell, E. 1991a, ApJ, 369, 395

—. 1991b, ApJ, 369, 395

MacNeice, P., Olson, K. M., Mobarry, C., de Fainchtein, R., & Packer, C. 2000, Computer Physics Communications, 126, 330

Mehringer, D. M., Palmer, P., Goss, W. M., & Yusef-Zadeh, F. 1993, ApJ, 412, 684

Olnon, F. M. 1975, A&A, 39, 217

Panagia, N. & Felli, M. 1975, A&A, 39, 1

Peters, T., Banerjee, R., Klessen, R. S., Mac Low, M.-M., Galván-Madrid, R., & Keto, E. R. 2010, ApJ, 711, 1017

Pratap, P., Snyder, L. E., & Batrla, W. 1992, ApJ, 387, 241

Press, W. H., Flannery, B. P., Teukolsky, S. A., & Vetterling, W. T. 1986, Numerical Recipes (Cambridge University Press)

Redman, M. P., Williams, R. J. R., & Dyson, J. E. 1996, MNRAS, 280, 661

Richling, S. & Yorke, H. W. 1998, A&A, 340, 508

Rijkhorst, E.-J., Plewa, T., Dubey, A., & Mellema, G. 2006, A&A, 452, 907

Rodríguez, L. F., Gómez, Y., & Tafoya, D. 2007, ApJ, 663, 1083

Rudolph, A., Welch, W. J., Palmer, P., & Dubrulle, B. 1990, ApJ, 363, 528

Truelove, J. K., Klein, R. I., McKee, C. F., Hollman II, J. H., Howell, L. H., & Greenough, J. A. 1997, ApJ, 489, L179

Van Buren, D., Mac Low, M.-M., Wood, D. O. S., & Churchwell, E. 1990, ApJ, 353, 570

Welch, W. J., Dreher, J. W., Jackson, J. M., Terebey, S., & Vogel, S. N. 1987, Science, 238, 1550

Williams, R. J. R., Dyson, J. E., & Redman, M. P. 1996, MNRAS, 280, 667

Wood, D. O. S. & Churchwell, E. 1989, ApJS, 69, 831

Xie, T., Mundy, L. G., Vogel, S. N., & Hofner, P. 1996, ApJ, 473, L131

Yorke, H. W. 1986, ARA&A, 24, 49